EXPERIMENTAL INVESTIGATION OF UAV ROTOR AEROACOUSTICS AND AERODYNAMICS WITH COMPUTATIONAL CROSS-VALIDATION

Anna A. Kostek[1], **Felix Lößle**[1], **Robin Wickersheim**[2], **Manuel Keßler**[2], **Ronan Boisard**[3], **Gabriel Reboul**[3], **Antonio Visingardi**[4], **Mattia Barbarino**[4], **Anthony D. Gardner**[1]

[1]German Aerospace Center (DLR), Göttingen, Germany
[2]University of Stuttgart (IAG), Germany
[3]French Aerospace Lab (ONERA), Meudon, France
[4]Italian Aerospace Research Center (CIRA), Capua, Italy

ABSTRACT

The study provided a base of comparison of known computational techniques with different fidelity levels for performance and noise prediction of a single, fixed-pitch UAV rotor operating with varying flight parameters. The range of aerodynamic tools included blade element theory, potential flow methods (UPM, RAMSYS), lifting-line method (PUMA) and Navier-Stokes solver (FLOWer). Obtained loading distributions served as input for aeroacoustic codes delivering noise estimation for the blade passing frequency on a plane below the rotor. The resulting forces and noise levels showed satisfactory agreement with experimental data, however differences in accuracy could be noticed depending on the computational method applied. The wake influence on the results was estimated based on vortex trajectories from simulations and those visible in Background Oriented Schlieren (BOS) pictures. The analysis of scattering effects showed that influence of ground and rotor platform on aeroacoustic results was observable even for low frequencies.

Abbreviations

APSIM	Aeroacoustic Prediction System based on Integral Methods
BEM	Boundary Element Method
BET	Blade Element Theory
BOS	Background Oriented Schlieren
BPF	Blade Passing Frequency
FW-H	Ffowcs Williams-Hawkings
PANGEN	Panel Generation code
PUMA	Potential Unsteady Methods for Aerodynamics
UAV	Unmanned Aerial Vehicle
UPM	Unsteady Panel Method
URANS	Unstady Reynolds-Averaged Navier--Stokes

1 Introduction

Unmanned aerial vehicles, like quadrocopters, have gained popularity due to their vertical take-off and landing (VTOL) and hover capabilities allowing operation in urban areas. Nevertheless, depending on the mission profile, the operation time of small UAVs may be mostly spent on forward flight [1, 2]. Therefore, optimisation of aerodynamic rotor design in regard to flight in edgewise flow could help to meet an ongoing challenge of increasing flight duration for electric UAVs. On the other hand, the developing UAV market is severely constrained by the public acceptance of the generated noise. While nowadays most multicopters are powered by electrical motors, it is the rotor that represents UAV's main noise source [3]. Although extensive studies have been done considering propellers operating under axial-flow conditions [4–8], their results are not applicable for forward flight with higher advance ratios. At the same time, the mechanisms acting on a small propeller in such conditions are not yet fully understood and cannot be directly derived from the full-size helicopter rotor. The main difference comes from the blade planform shape, as multicopters are typically driven by rigid blades with non-linear twist distribution and strong chord variation along the span [6]. As advancing and retreating side effects are not compensated, like in the case of hinged helicopter rotors, a fixed-pitch propeller in forward flight experiences high thrust fluctuations throughout the rotation, which also results in an asymetry of the produced wake [9]. Additional complexity arises when small-size propellers operate at low Reynolds num-

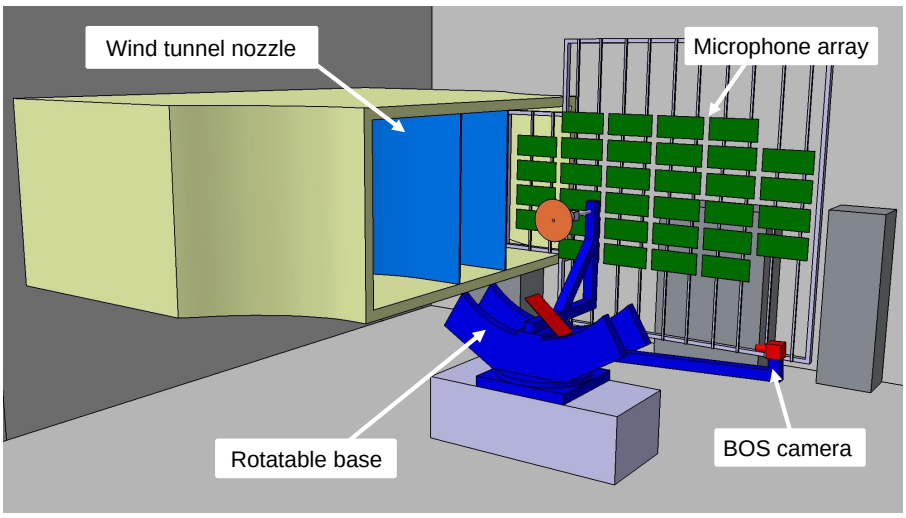

Figure 1: Experimental setup

bers, which has impact on both performance [10–12] and noise generation [13].

As a result, accurate aerodynamic and aeroacoustic prediction tools, capable of handling specifics of small rotors in forward flight are necessary. From aerodynamic methods described in the literature, models based on blade element theory (BET) are the most simplified and time-efficient, yet for many cases they show accuracy comparable with higher-fidelity solvers [8, 14, 15]. For this reason, they are commonly used as an initial loading estimation during the design process [3,7]. BET methods require external estimation of inflow velocities, which can be derived from momentum theory for cases like hover or axial climb, however forward flight calculations typically involve more complicated models [16]. Methods based on potential flow represent a complexity between BET models and RANS solvers. Their great advantage is the ability to simulate unsteady conditions, while ensuring time-efficiency [9]. Potential methods are usually coupled with a free-wake method, as described in [17] but can also include extensions for viscous particle wake [18] or post-processing viscous and compressible corrections.

In recent years a few studies have been dedicated to the experimental research of small propeller's performance in edgewise flight, like [19, 20], also including aeroacoustic measurements [2, 21]. Studies described in [9] showed the application of potential flow method for such conditions. Other studies [1, 15] juxtaposed results from various aerodynamic tools together with experimental data.

This study, prepared within the GARTEUR Action Group 25, compares solvers with different fidelity levels including BET, potential flow methods (UPM, RAMSYS), lifting-line method (PUMA) and Navier-Stokes solver (FLOWer) regarding load-prediction, but also examines their applicability as a base for noise estimation.

2 Experimental setup

The experiment involved aerodynamic and aeroacoustic measurements and was conducted in the Rotor Test Facility Göttingen (RTG) of the German Aerospace Center (DLR) with a setup presented in Figure 1. The aeroacoustic array was positioned 1.35 m below the rotor plane and consisted of 512 MEMS (micro-electrical-mechanical systems) microphones (Fig. 2). Presented noise levels were corrected based on the measurements with loudspeaker emitting white noise to compensate for the effects connected with room acoustics. Thrust and torque were measured with a strain-gauge and piezoelectric balance, respectively.

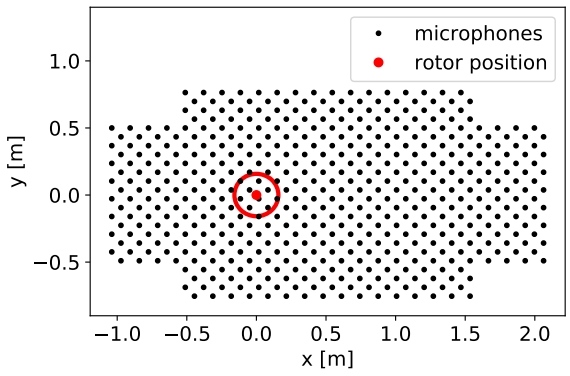

Figure 2: Microphone positions relative to rotor plane

The measurements included variations in flight velocity, rotor RPM and tilt angle. However, special focus was put on a case presenting the effect of a change in rotor inclination between -30° and 30° (Fig. 3) with fixed flight velocity and rotational speed (advance ratio 0.146). Vortex trajectories were detected by the Background Oriented Schlieren (BOS) method using a high-speed camera, reflecting mirror and dotted

background mounted above the propeller. A detailed description of the experimental setup can be found in [22].

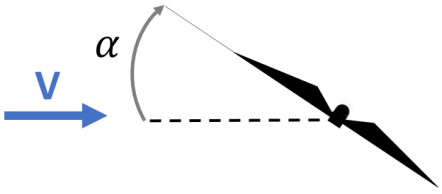

Figure 3: Tilt angle sign convention

3 Geometry

A 2-bladed, fixed-pitch KDE 12.5x4.3" rotor with 0.318 m diameter and solidity 0.075 was used. Computational models were prepared based on a 3D-scanned blade, divided into series of spanwise cuts (Fig. 4). Figure 5 presents the obtained twist and chord distributions. Due to inaccuracies of a scanned surface, 4-digit NACA profiles were identified to approximate a hydraulically smooth airfoil shape at the measured cross sections [23]. The shape of the trailing edge could be adjusted depending on the computational method applied (Fig. 6).

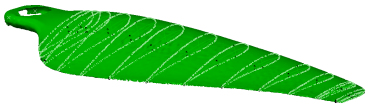

Figure 4: Scanned blade with cross-sections

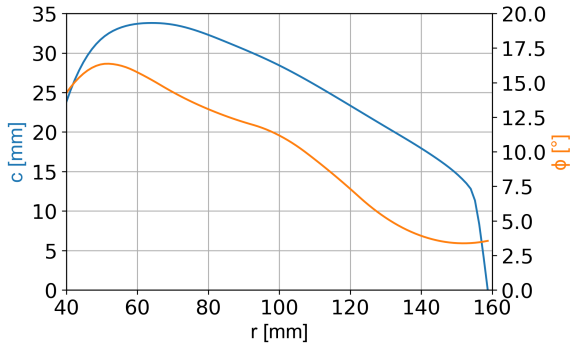

Figure 5: Twist and chord distributions

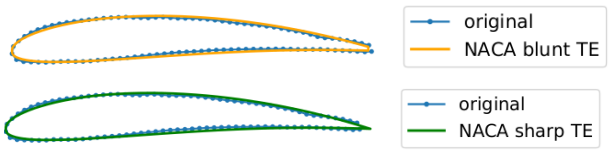

Figure 6: Example - trailing edge shapes of recreated profiles

4 Computational methods

4.1 BET and FW-H code

The blade element theory (BET) represents the most simplified and the least computationally expensive of the applied methods. In BET, steady lift and drag values are calculated for spanwise blade sections at different azimuthal positions and then integrated for the whole rotation. A value of the inflow angle and the corresponding angle of attack can be determined iteratively from a loop with an inflow model. A dedicated Python code used in this study included a linear inflow model developed by Pitt and Peters [24] (Fig. 7). Aerodynamic characteristics for airfoils identified for each spanwise cut were prepared using XFOIL and considered variation of Reynolds and Mach numbers. Lift and drag coefficients were then extrapolated for high angles of attack with the post-stall Viterna model [25] (Fig. 8). The BET code did not include wake model. Two ways of including tip-loss effects were investigated, either by adding Prandtl's function to the solution or by estimating a tip-loss factor B as a constant value (as described in [17] typically between 0.95 and 0.98). The Prandtl's function approach lead to strong underestimation of thrust values for a rotor operating in strong upwash (positive tilt angles), therefore in the presented results a B factor was simply approximated as 0.97 and mean thrust values were reduced by a factor B^3 for forward flight cases [26].
As the final step, the resulting loading distribution served as an input for a coupled aeroacoustic prediction code based on the Ffowcs Williams-Hawkings (FW-H) equation with the Farassat 1A formulation, as described in [3]. Only loading noise was taken into account in the acoustic calculation.

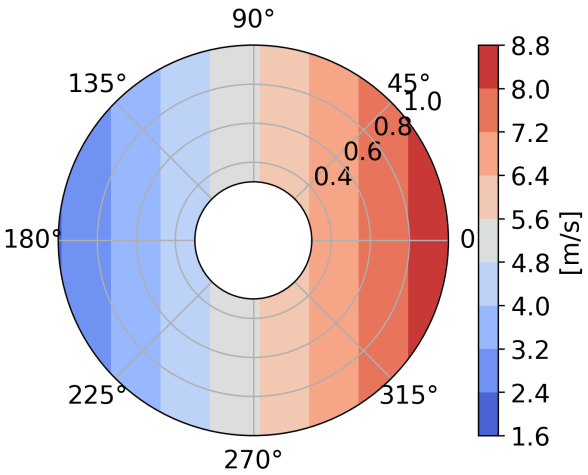

Figure 7: Induced velocity distribution with Pitt and Peters model for 5400 RPM, 12.9 m/s, tilt -10°

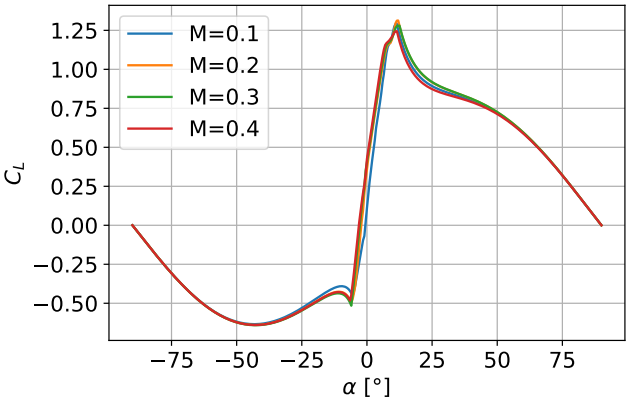

Figure 8: Viterna extrapolation of lift coefficient for higher angles of attack used in the BET code

4.2 UPM and APSIM

UPM is an unsteady free-wake panel method developed at DLR allowing the simulation of flows with arbitrary body shape and motion [27,28]. The code solves potential flow, although viscosity and compressibility effects can be included in post-processing. A viscous correction, applied to improve the estimation of torque values, estimates the contribution of profile torque using equation (1) [26], where section zero-lift drag coefficient C_{d_0} has a default value of 0.0075, σ and μ stand for rotor solidity and advance ratio, respectively.

$$C_{Q_0} = \frac{\sigma C_{d_0}}{8}(1 + 1.5\mu^2 - 0.37\mu^{3.7}) \quad (1)$$

Lifting bodies in UPM are modelled as a distribution of sources and sinks on the blade surface accounting for the displacement effect and doublet distribution along the chord simulating the lift. The weighting function of doublet strength is prescribed and depends on the profile thickness. An iterative scheme to ensure pressure equality at the trailing edge and satisfy the Kutta condition was applied in the calculations. The panel generation code PANGEN served in this study as a tool to prepare a computational model of meshed blade with finite thickness and sharp trailing edge (Fig. 9). The full span free wake of the blades mostly used a vortex lattice, yet additional calculations were carried out using particle wake method, in which the vortex filaments are replaced by point vortices (Fig. 10). The particle model solves the vorticity transport equation derived from the incompressible Navier-Stokes equations. As there are no connections between the neighbouring particles, this approach enables an improved solution for cases where the wake interferes with solid bodies. Calculations were carried out for approximately 8 rotations with step size reduced from 5° to 2° after 5 rotations.
A coupled code APSIM (Aeroacoustic Prediction System based on Integral Methods) [29] takes into account linear sound propagation and includes two integral formulations of FW-H equation for an permeable and impermeable surface. The latter approach was used in this study based on pressure distribution on the blade surface from the last rotation calculated in UPM.

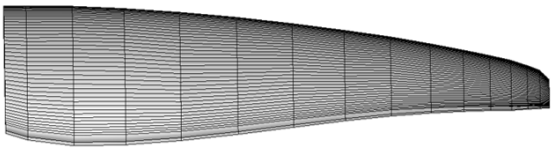

Figure 9: Distribution of panels on a blade surface from UPM

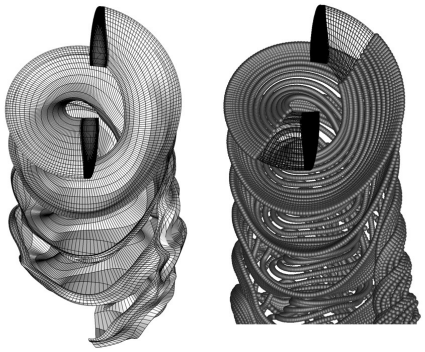

Figure 10: Wake represented in UPM with vortex lattice (left) and vortex particles (right)

4.3 PUMA and KIM

PUMA (potential unsteady methods for aerodynamics) is an unsteady lifting line / free-wake solver developed at ONERA since 2013. It includes a coupling between an aerodynamic module and a kinematic module. The aerodynamic module uses the lifting line method with a free-wake model based on Mudry theory [30], which describes the unsteady evolution of a wake modelled by a potential discontinuity surface. The lifting line method is based on two-dimensional (2D) airfoil characteristics through lookup tables. It can handle some 3D corrections for blade sweep and 2D unsteady nonlinear aerodynamics effects through dynamic stall models. Moreover, different time discretizations are available in order to balance between accuracy, numerical stability and computational time. The kinematic module employs a rigid multi-body system approach using a tree-like structure with links and articulations. It enables any arbitrary motion between the different elements. PUMA is usually used for any aerodynamic study of fixed wings and rotating wings configurations which require low computational cost or a large amount of parametric investigations like pre-design studies. It has also been successfully applied for helicopter rotors wake in interactions with obstacles [31, 32] and for rotor / rotor

interactions [33].
In this study, the 2D airfoil characteristics are the same as the ones used in the BET method. The lifting line is divided into 45 radial stations for wake emission using a square root distribution. A time step of 5° was used for the unsteady computation over 8 rotor revolutions. The unsteady spanwise distribution of loads obtained using PUMA are empirically distributed in terms of pressure on the entire blade surface and are then used by the KIM code [34, 35] to determine the noise emission. KIM is based on a Ffowcs-Williams and Hawkings formulation implemented in an advanced time approach.

4.4 FLOWer and ACCO

For high fidelity simulation the numerical process chain used at the IAG was applied. CFD results are generated with the structured code FLOWer, originally developed by DLR [36] and further developed at the Institute of Aerodynamics and Gas Dynamics at the University of Stuttgart [37]. Acoustic coupling was provided by IAG's FW-H solver ACCO [38] with usage of the data output of FLOWer. A second order dual time stepping for temporal evolution was used with a time step of 1° to resolve the acoustic waves. Furthermore, the Menter-SST turbulence model was applied to close the URANS equations. For spatial discretization the surface of the propeller was meshed with 0.1% of the chord length in streamwise direction. To recognize tip effects mesh refinement up to 1% of the radius in spanwise direction was set. Using the Chimera technique a separate background mesh was created utilizing hanging grid nodes to reduce the numerical expense. Furthermore, in all background volume cells the WENO scheme of 6^{th} order is carried out for numerical stability and reduced dissipation. In the surface region the dimensionless wall distance is kept low at $y^+ < 1$. The λ_2-criterion for vortex visualization and numerical setup are shown in Figure 11 and 12, respectively.

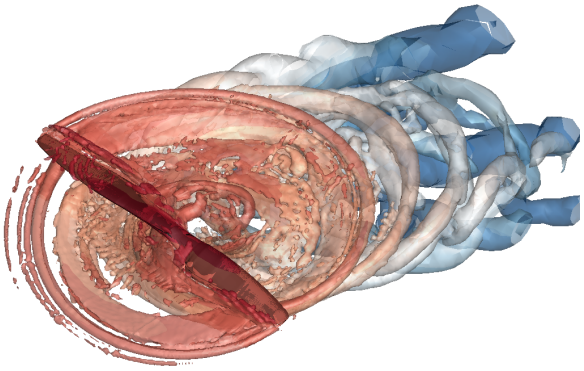

Figure 11: Wake visualized in FLOWer using λ_2-criterion

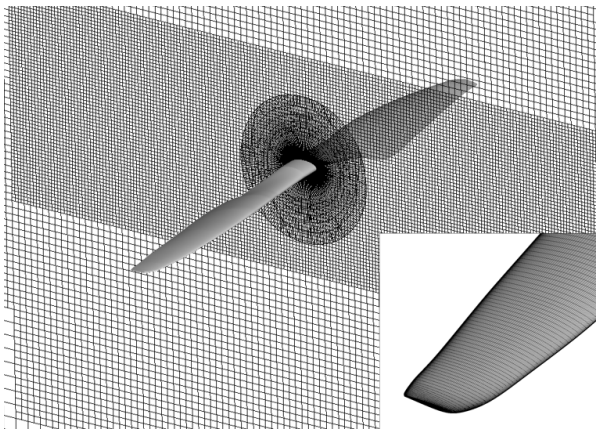

Figure 12: Numerical setup in FLOWer – background and propeller mesh with chimera interpolation

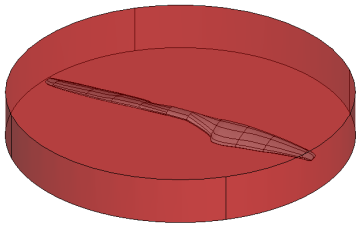

Figure 13: Integration surface for acoustic coupling as input for ACCO and physical surface of the rotor blade

The acoustic code ACCO uses an acoustic integration surface, within which sound is generated by the fluid. The integration is accomplished on a cylindrical permeable surface (red in Fig. 13) to enclose all sound sources. The selection of the spatial discretization in the background mesh was based on the resolution of the first harmonic wave length, with 20 cells discretizing the wave length of the blade passing frequency (BPF). To avoid excessive dissipation the integration surface is placed in the finest grid area without cell size changes.
The scattering effects described in Section 6.1 were computed using the Boundary Element Method (BEM) tool ScatMan [39] developed at the Institute of Aerodynamics and Gasdynamics [40]. Within the ScatMan tool, the sound propagation in the frequency domain is described by the Helmholtz equation, expanded with Green's second theorem resulting in the Helmholtz-Kirchoff equation [40]. To include ScatMan in the numeric tool chain consisting of FLOWer and ACCO, the shielding had to be discretized in triangle elements. ACCO in the first step calculates the incident sound pressure at the discrete points on the surface of the shielding as well as in a small distance above each surface point. Afterwards, the ambient conditions are added resulting in the complete solution consisting of acoustic and scattering field.

4.5 RAMSYS and ACO suite

The CIRA aerodynamic simulations were carried out by using the medium-fidelity code RAMSYS [41], which is an unsteady, inviscid and incompressible free-wake vortex lattice boundary element methodology (BEM) solver for multi-rotor, multi-body configurations developed at CIRA. It is based on Morino's boundary integral formulation [42] for the solution of Laplace's equation for the velocity potential φ. The surface pressure distributions are evaluated by applying the unsteady version of Bernoulli equation, which is then integrated to provide the forces and moments on the configuration and the surrounding obstacles. A computational acceleration is obtained by applying the module for symmetrical flows and geometries implemented in the solver and the parallel execution via the OpenMP API. The aeroacoustic simulations were carried out by using the ACOustic suite developed at CIRA and consisting of several tools for the evaluation of noise generation and propagation. The ACO-FWH solver is used for computing the acoustic free-field generated by the rotor blades. It is based on the FW-H formulation [43] described in [44, 45]. The advanced-time formulation of Farassat 1A is employed, and the linear terms (the so-called thickness and loading noise contributions) are computed through integrals both on the moving blades surface (impermeable/rigid surface formulation). Moreover, the space derivatives of the linear terms are also evaluated through a numerical integration for coupling the free-field solution computed with FW-H with scattering solvers [46]. The quadrupole contribution due to the nonlinear terms distributed in the perturbed field around the blade is neglected. The computational acceleration is obtained by a parallel execution via the MPI API. The simulation of the aeroacoustic free-field was carried out by using the aerodynamic database evaluated by RAMSYS, and consisting of the rotor blade pressure distributions. The ACO-FAM solver was used for the simulation of the acoustic scattering field. It is based on the numerical solution of the convected Helmholtz equation which can be handled with an integral boundary element formulation [47]. ACO-FAM implements the aforementioned integral boundary element formulation for the solution of interior and exterior acoustic problems (radiation and scattering) and solves the inverse problem through a collocation with the BEM. The ACO-ENV solver implements the acoustic propagation of a generic noise source through a ray approximation as described in [48]. This solver allows for the computation of several noise metrics starting from the definition of the flight trajectory and the noise source database encompassing the flight envelope. Moreover, it is able also to account for single reflections and attenuation by barriers or buildings. Single reflections are managed through an analytical mirroring of the source whereas the attenuation is managed through semi-analytical formulations [49, 50].

5 Results

5.1 Aerodynamic loading prediction

A comparison of time-averaged thrust and torque values presented in Figures 14-16 indicates that general tendencies captured in the measurements are reproducible using all computational tools, however some differences can be noticed in terms of accuracy. It is worth mentioning that for moderate flight velocities BET solution offers good loading estimation, even with simplified assumptions considering tip-loss factor. As the same 2D airfoil characteristics were used as an input for BET and PUMA, the loading calculated with these both methods is similar in Figures 14-15 and for low tilt angles in Figure 16. The accuracy of these solvers becomes worse for low advance ratios (Fig. 15), which can be explained by the limitations of XFOIL for calculating cases with very small Reynolds numbers and omission of rotational effects in the airfoil data. For most of the analysed points underprediction of torque values is expected from potential flow solvers, like UPM or RAMSYS caused by neglection of viscosity effects. A post-processing correction in UPM estimating the contribution of profile drag considerably improved the agreement between calculated and measured torque values. The assumption of inviscid flow lead to the underestimation of torque by at least 10% for most of presented cases.

With the rotor tilted backwards, the interaction with vortices becomes dominant and the lines from BET and PUMA diverge, as the BET code did not include a wake model in the solution (Fig. 16(b)). The increase in interactional effects between positive and negative rotor inclinations can be observed in Figure 18 presenting wake visualizations and from unsteady loads depicted in Figure 17. For negative tilt angles, like in Figure 18(a), the horizontal component of the velocity induced by the propeller is in the direction of the free stream velocity and the vertical component pushes the wake downward away from the propeller. This combination of velocities causes a rapid convection of the wake downstream. As a consequence, there is little interaction between the wake and the propeller, the unsteadiness is moderate and so are the effects on the loads acting on the propeller disk (Fig. 17(a)). Figure 18(b) shows the wake developed at a positive tilt angle. In this case, the horizontal component of the velocity induced by the propeller is opposite to the free stream velocity. This not only reduces the convection process downstream but also causes the wake to be fully ingested by the propeller disk with the resulting generation of high interactional effects giving rise to unsteady loads (Fig. 17(b)). The flight regime of a rotor operating in strong upwash transitions towards windmill state, where the blades are driven by the flow, explains the rapid decrease in torque values in Figure 16(b). For FLOWer and PUMA this transition appears

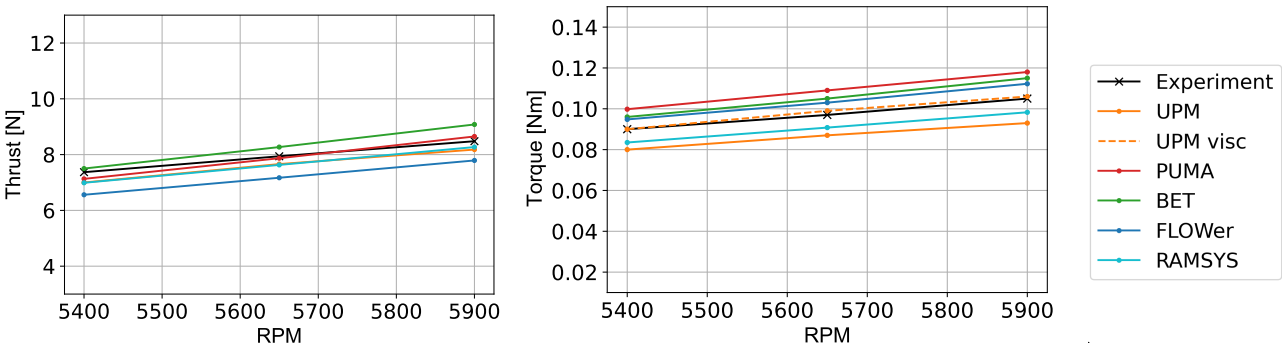

(a) RPM effect on rotor thrust (b) RPM effect on rotor torque

Figure 14: Results for varying rotor RPM with fixed flight velocity of 12.9 m/s and tilt angle -10°

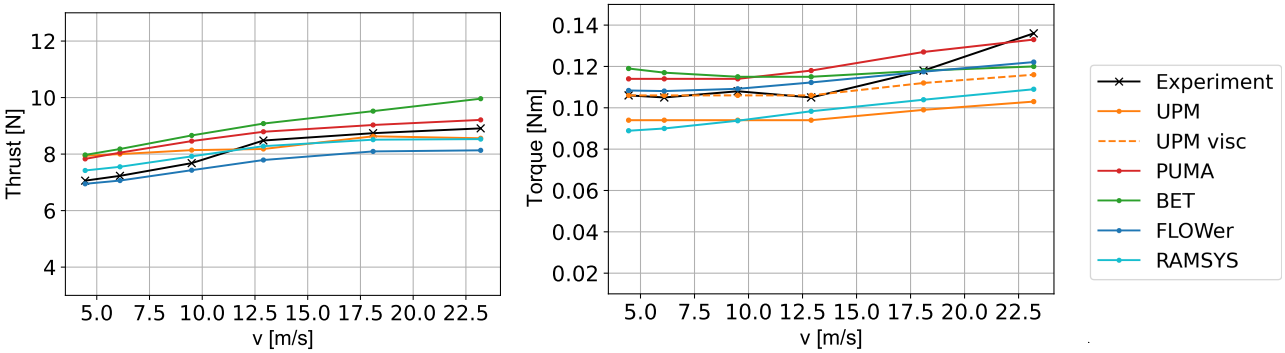

(a) Velocity effect on rotor thrust (b) Velocity effect on rotor torque

Figure 15: Results for varying rotor velocity with fixed 5900 RPM and tilt angle -10°

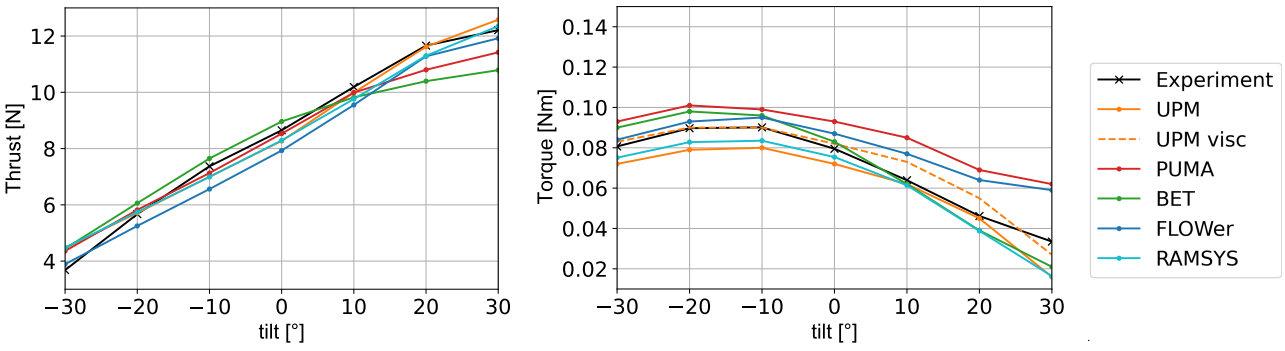

(a) Tilt effect on rotor thrust (b) Tilt effect on rotor torque

Figure 16: Results for varying rotor tilt angle with fixed 5400 RPM and flight velocity 12.9 m/s

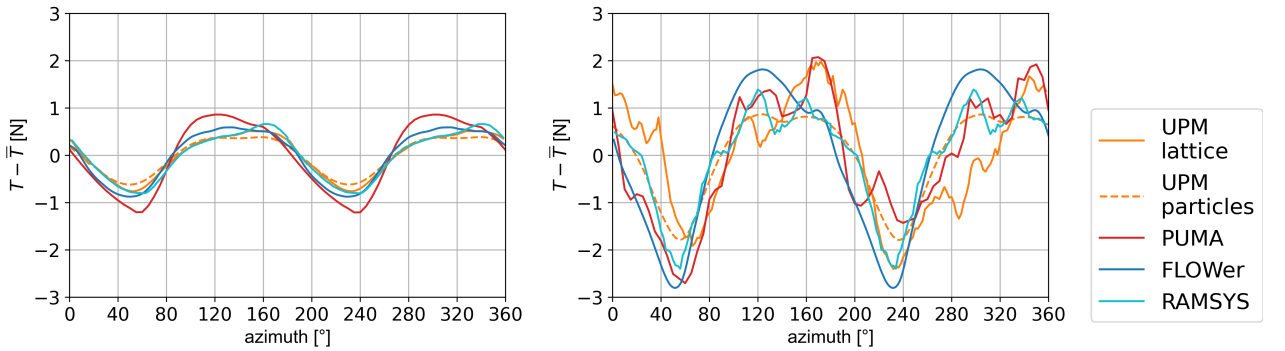

(a) Tilt -10° (b) Tilt 20°

Figure 17: Thrust fluctuations during one rotation for 5400 RPM and flight velocity 12.9 m/s

slower in comparison with other solvers, which is connected with an overestimation of viscous effects in this region by these solvers.

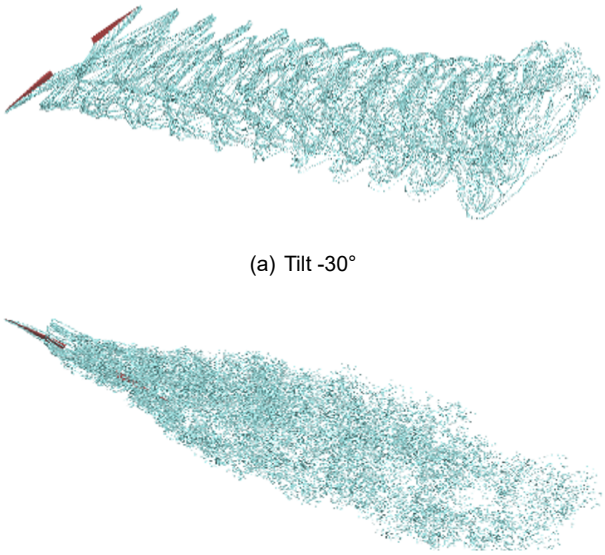

(a) Tilt -30°

(b) Tilt 30°

Figure 18: Propeller wake system development for different tilt angles simulated in RAMSYS

Additionally, Fig. 17 presents a comparison of unsteady loading for chosen tilt angles calculated in UPM with vortex lattice and vortex particles. Although the discrepancy between time-averaged thrust values calculated with these both methods was negligible, an apparent difference can be noticed in thrust fluctuations for positive angles of attack (here 20°), for which the particle method offers a more stable solution. This can be explained by the distortion of the vortex lattice wake when straight line filaments cross blades and singularity problems appearing when wake panels are too close to each other.

The loading calculated using BET differs in phase compared with results from other methods. According to the BET code the maximum thrust is reached around azimuth 90°, which is where the calculated relative velocity coming from the rotational motion of the blade and flight velocity reaches the highest value. For all other results the thrust peak appears around 40° later, more to the front of of the rotor disc. This tendency is due to unsteady effects, which are not covered by a simplified inflow model and originate mostly from the wake presence, as shown in Figure 19. The phase delay can be partially corrected by means of Theodorsen's theory, that accounts for unsteady development of lift, as described in [17]. In Figure 19 phase shift resulted from Theodorsen's function was averaged throughout the disc for each blade section and used to correct the initial result. The applied correction helped to include a case-dependent time delay in the BET solution, however it did not ensure complete compatibility with other solvers. A comparison between BET and the UPM result without a wake, shows that the time delay can be modelled using the free wake, which is missing in the BET code. In this study, Theodorsen's function served only as a quick estimation, as the main objective was to investigate the possible applications of basic BET assumptions.

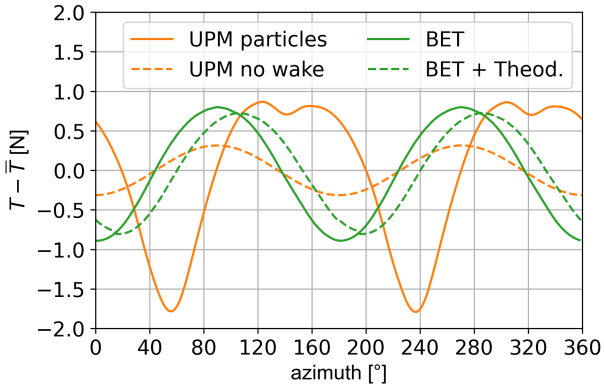

Figure 19: Time signal of thrust for tilt 20° during one rotation with 5400 RPM and flight velocity 12.9 m/s

5.2 Noise prediction

Aerodynamic results indicate that the effect of tilt change with the other parameters kept fixed had the largest effect on the rotor loading (compare Fig. 14, 15 and 16). For this reason, the aeroacoustic study was focused on cases with constant velocity 12.9 m/s and rotational speed of 5400 RPM with a range of rotor inclinations, as analysed in Figure 16. Noise carpets were prepared based on the calculated loadings using several acoustic solvers described in Section 4. The focus of the analysis was put on the blade passing frequency as it had a dominant influence on noise levels.

The noise directivity pattern for cases with forward tilt of the rotor (see Fig. 20) is similar for all of the computational methods. However, the accuracy of results depended on fidelity levels of applied tools with the ACCO solution closest to the experimental data. The noise carpet calculated with BET+FW-H shows agreement with other methods, what indicates that the wake had no great influence in these range of tilt angles and that the main noise contribution came from the loading noise. Interestingly, the phase discrepancy observed for unsteady loading calculated with BET did not considerably influence the quality of the result.

As expected, for higher tilt angles the loading increases and so do noise levels on all calculated carpets. However, the difference in directivity between the outcome of BET and other methods can be noticed (Fig. 21). This tendency no longer occurred for the highest backward inclination of the rotor as presented in Figure 22. An explanation of this phenomenon can

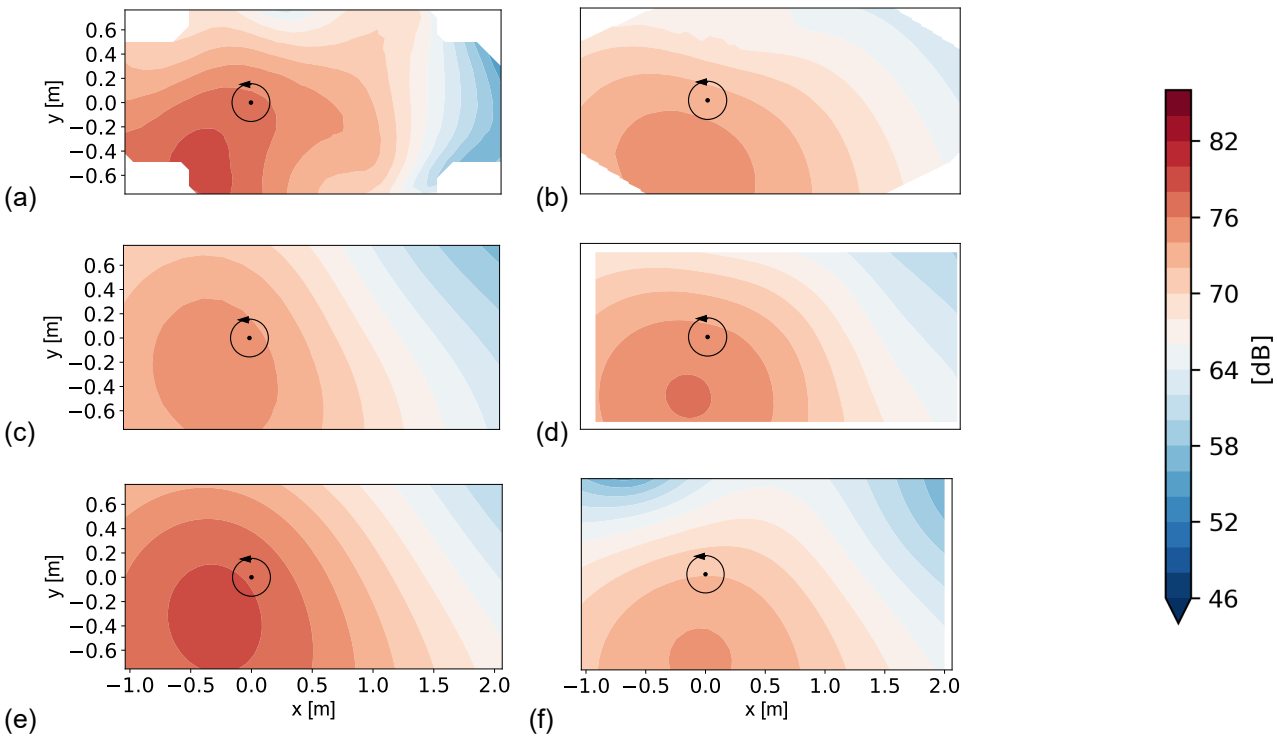

Figure 20: Noise carpets of the BPF, 5400 RPM, flight velocity 12.9 m/s, tilt angle -10°. (a) Experiment, (b) UPM+APSIM, (c) BET+FW-H, (d) FLOWer+ACCO, (e) PUMA+KIM, (f) RAMSYS+ACO

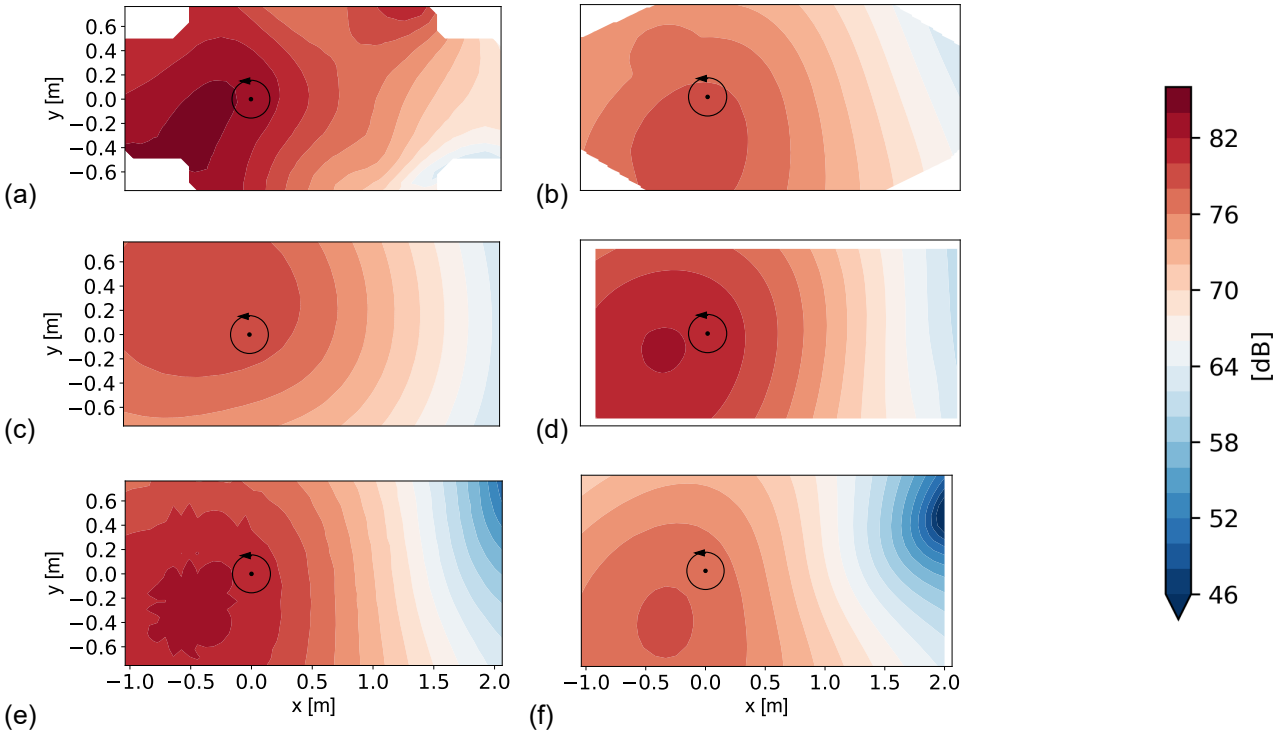

Figure 21: Noise carpets of the BPF, 5400 RPM, flight velocity 12.9 m/s, tilt angle 20°. (a) Experiment, (b) UPM+APSIM, (c) BET+FW-H, (d) FLOWer+ACCO, (e) PUMA+KIM, (f) RAMSYS+ACO

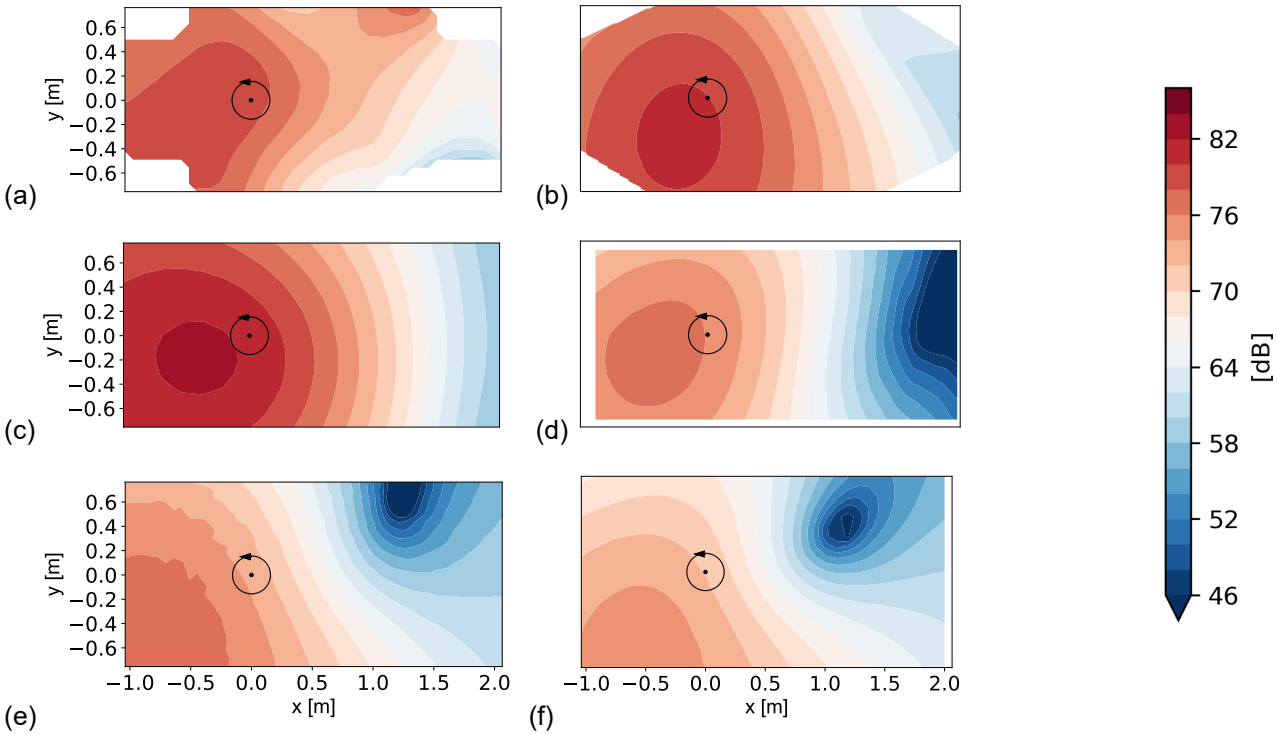

Figure 22: Noise carpets of the BPF, 5400 RPM, flight velocity 12.9 m/s, tilt angle 30°. (a) Experiment, (b) UPM+APSIM, (c) BET+FW-H, (d) FLOWer+ACCO, (e) PUMA+KIM, (f) RAMSYS+ACO

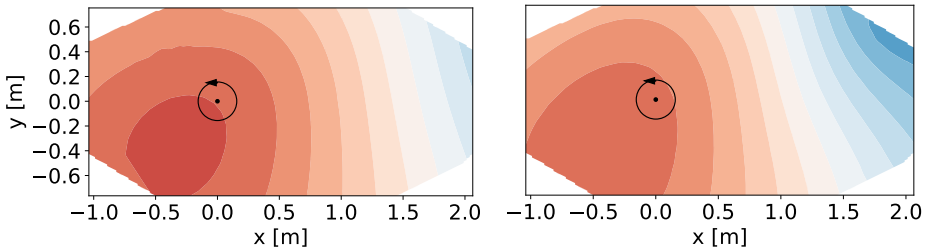

(a) Tilt 20° (b) Tilt 30°

Figure 23: Noise carpets from UPM with particle wake + APSIM (colorbar like in Fig.22)

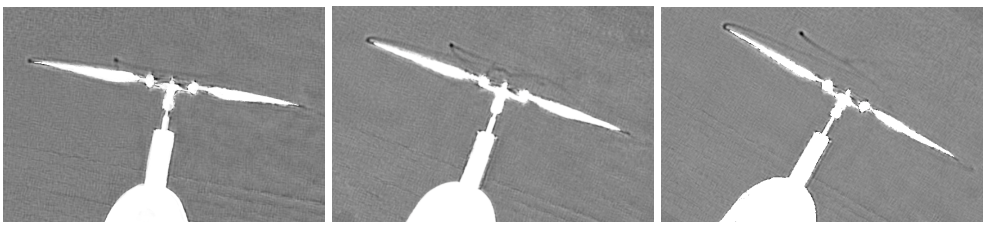

(a) BOS, Tilt 10° (b) BOS, Tilt 20° (c) BOS, Tilt 30°

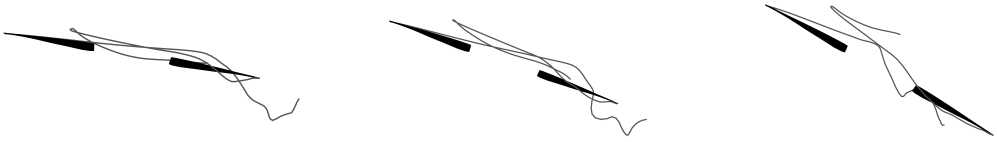

(d) UPM, Tilt 10° (e) UPM, Tilt 20° (f) UPM, Tilt 30°

Figure 24: Vortex trajectories detected in BOS pictures and UPM wake visualizations

be found in vortex trajectories detected in (BOS) pictures and also visible in UPM visualizations (Fig. 24). The marked positions of tip vortices for moderate positive tilt angles were always located in the proximity of the blades, strongly affecting rotor loading (Fig. 24(d), 24(e)). For 30° the vortices tend to move away from the rotor plane, therefore, the result of BET neglecting wake influence again agreed with the measurement. This observation could also explain why the highest noise levels were measured for a tilt angle of 20° even though the highest loading can be observed for 30° inclination.
With the propeller tilted backwards, more differences in calculated noise levels between analysed methods can be observed, which is connected to increased unsteadiness in the flow and decrease of stability of numerical solutions. For these cases also a discrepancy between the aeroacoustic results based on loading prepared with vortex lattice and vortex particles in UPM can be observed (compare Figures 21(b) and 22(b) with 23), as high time derivatives of thrust did not appear in the latter (Fig. 17).

6 Scattering effects

Although the calculated noise carpets showed satisfactory agreement with experimental data in the vicinity of the rotor, none of completely captured measurement results with the highest deviations observed further behind the rotor. Reasons for this can be found by evaluating the influence of scattering effects at the aerodynamic shielding, rotatable rotor base and ground.

6.1 Influence of the shielding

An acoustic study was carried out to observe the influence of the scattered field caused by the aerodynamic shielding placed beneath the rotor during the measurements (Fig. 25). For 5400 RPM and velocity 12.9 m/s a case with tilt angle of -10° was chosen for the investigation as in these conditions propeller wake is expected to interfere the most with the shielding. Calculations were conducted using ScatMan tool described in Section 4.4 with an assumption of a hard shielding surface ($v_n = 0$).
Figure 26 shows that acoustic wave reflection caused an increase of up to 2 dB for the BPF on the upstream side of the shielding surface, as well as decrease of around the same value on the downstream side. However, as the dimensions of the shielding are much smaller than the wavelength of the blade passing frequency (3.8 m) sound waves reflected by the shielding caused a negligible deviation in the noise field, which can be observed comparing Figure 27 with the baseline numerical approach in Figure 20(d). Additionally, as the presence of the shielding did not cause a change of more than 3% in the thrust values computed for chosen cases in UPM, the baseline approach to neglect its aerodynamic and aerodynamic influence in the calculations is justifiable.

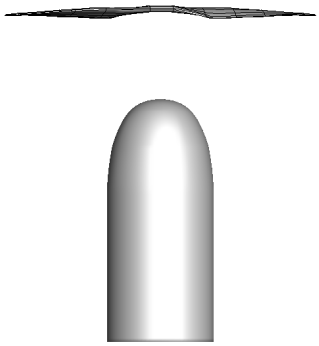

Figure 25: Propeller included in CFD simulation and shielding element implemented in the Scatman tool

6.2 Installation and ground proximity effects

Further scattering effects were evaluated using ACOFAM solver as described in Section 4.5. The computational setup included the part of ground and the platform on which the propeller was mounted (Fig. 28). The integration surface used for FW-H and BEM calculation is presented on Fig. 29. Calculations were conducted for tilt angles -10° and 20°, 5400 RPM and flight velocity 12.9 m/s. As the dimensions of the analysed objects are in the order of the acoustic wavelength, their influence can be observed in the noise carpets of the blade passing frequency. The acoustic fields including scattering effects (Fig. 30) show a visible difference in both noise directivity and noise levels in comparison with base results from Figure 20(f) and Figure 21(f). Depending on the case and the analysed location the presence of the ground and rotor platform caused either an increase (Fig. 30(b)) or decrease in the noise levels (Fig. 30(a)).

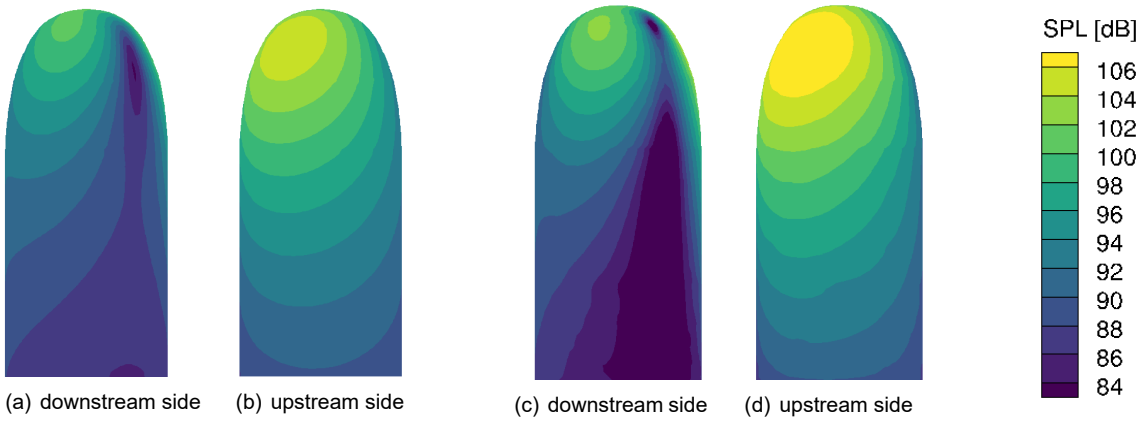

Figure 26: Acoustic field for the BPF on the shielding surface including incident noise (a),(b) and the sum of incident and scattered noise (c),(d) for 5400 RPM, flight velocity 12.9 m/s, tilt angle -10°

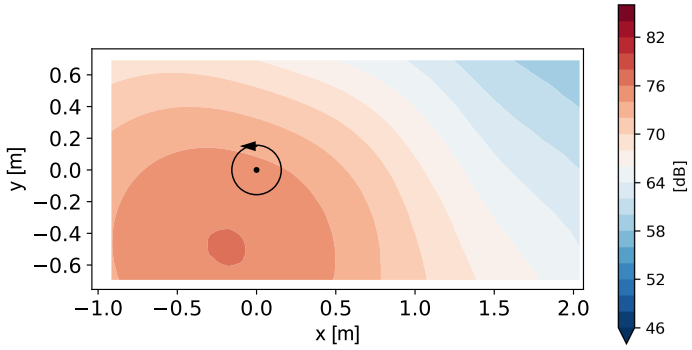

Figure 27: Noise carpet including total (incoming and scattered by the shielding) sound pressure level of the blade passing frequency - FW-H + ScatMan for 5400 RPM, flight velocity 12.9 m/s, tilt angle -10°

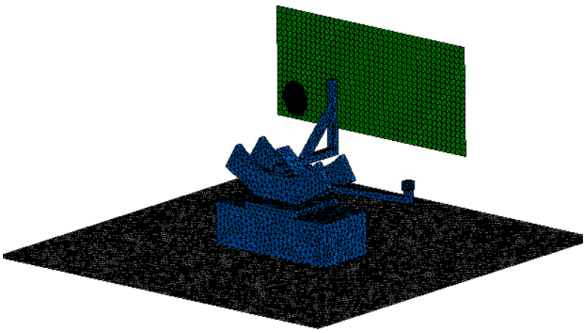

Figure 28: Acoustic mesh for BEM calculation

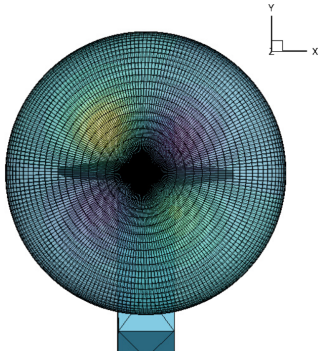

Figure 29: Integration surface for FW-H and BEM

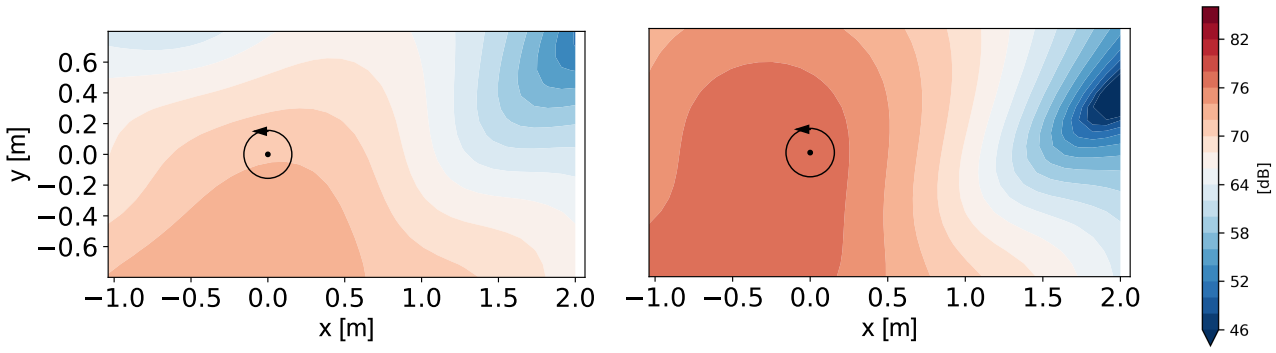

Figure 30: Scattering effects for 5400 RPM and flight velocity 12.9 m/s

7 Conclusions

Aeroacoustic and aerodynamic calculations were performed, indicating that measurement results for most cases were reproducible with satisfactory agreement by all computational methods, regardless of their fidelity level. The most basic and time-efficient BET shows compatibility with other tools for moderate flight velocities and propeller tilt angles, when it comes to time-averaged results, yet the code is not a reliable tool for reproducing transient loading. The BET approach loses credibility for cases where a three-dimensional wake influence becomes dominant, like flow with backward inclination of the propeller. An accurate result for such conditions can be achieved with methods including wake in the solution, from which codes incorporating viscous effects (like FLOWer, UPM with particle wake) offer more stability. The BET solution regained applicability for the highest analysed tilt angle of 30°, when wake vortices move further downstream from the blades.

Airfoil characteristics used in BET and PUMA allow for including the influence of compressibility and viscosity in the solution. However, one needs to be aware of XFOIL limitations when it comes to accuracy for low Reynolds numbers and lack of consideration of rotational effects in this approach.

Mid-fidelity solvers based on potential flow (UPM, RAMSYS) ensured high accuracy of thrust values for cases, where blades do not operate at stall conditions. However, the assumption of inviscid flow leads to strong underprediction of torque. A simple post-processing correction accounting for profile drag significantly improved the quality of results.

Except for the BET+FW-H solution for tilt angle 20°, calculated noise carpets of the blade passing frequency agreed with the measurement when it comes to the location of the highest noise level. Deviations in the results were more apparent for positive tilt angles and appeared for the area further downwash behind the rotor hub. Objects like rotor base or ground with dimensions comparable with the wavelength caused reflections affecting acoustic results. Although the noise carpets including analysed scattering effects still do not explain all deviations in the acoustic measurements, they clearly indicate the importance of reflections analysis, even for low frequencies.

8 Acknowledgments

The study was funded by the German Aerospace Center (DLR) as a part of the Urban Rescue project. Cooperation between research facilities was enabled within the group GARTEUR AG-25 “Rotor-rotor wakes Interactions”.

References

[1] Theys B, Dimitriadis G., Hendrick P., De Schutter J.: Experimental and Numerical Study of Micro-Aerial-Vehicle Propeller Performance in Oblique Flow. Journal of Aircraft, Vol. 54, No. 3 (2017)

[2] Yang Y., Liu Y., Li Y., Acrondoulis E.: Aerodynamic and Aeroacoustic Performance of an Isolated Multicopter Rotor During Forward Flight. AIAA Journal, Vol. 58, No.3 (2020)

[3] Gur O., Rosen A.: Design of a Quiet Propeller for an Electric Mini Unmanned Vehicle. Journal of Propulsion and Power, Vol. 25, No. 3 (2009)

[4] Ning Z., Hu H.: An Experimental Study on the Aerodynamic and Aeroacoustic Performances of a Bio-Inspired UAV Propeller. AIAA Aviation Forum (2017)

[5] Ning Z., Hu H.: An Experimental Study on the Aerodynamics and Aeroacoustic Characteristics of Small Propellers. AIAA Science and Technology Forum an Exposition (2016)

[6] Deters R.W., Kleinke S.: Static Testing of Propulsion Elements for Small Multirotor Unmanned Aerial Vehicles. 35th AIAA Applied Aerodynamics Conference (2017)

[7] Weitsman D.,Greenwood E.: Parametric Study of eVTOL Rotor Acoustic Design Trades. Pennsylvania State University (2021)

[8] Gur O., Rosen A.: Comparison Between Blade-element models of Propellers. The Aeronautical Journal, Vol.112, No. 1138 (2008)

[9] Krebs T., Bramesfeld G., Cole J.: Transient Thrust Analysis of Rigid Rotors in Forward Flight. (2022)

[10] Deters R.W., Ananda G.K., Selig M.S.: Reynolds Number Effects on the Performance of Small-Scale Propellers. 32nd AIAA Applied Aerodynamics Conference (2014)

[11] Gur O., Rosen A.: Propeller Performance at Low Advance Ratio. Journal of Aircraft. Vol. 42, No. 2 (2005)

[12] McCrink M.H., Gregory J.W.: Blade Element Momentum Modelling of Low-Re Small UAS Electric Propulsion Systems. 33rd AIAA Applied Aerodynamics Conference (2015)

[13] Grande E. et al.: Aeroacoustic Investigation of a Propeller Operating at Low Reynolds Numbers. AIAA Journal, Vol. 60, No. 2 (2022)

[14] Bergmann O., Götten F., Braun C., Janser F.: Comparison and evaluation of blade element methods against RANS simulations and test data. CEAS Aeronautical Journal 13:535-557 (2022)

[15] Cerny M., Herzog N., Faust J., Stuhlpfarrer M., Breitsamer C.: Systematic Investigation of a Fixed-pitch Small-scale Propeller under Non-axial Inflow Conditions. Deutscher Luft- und Raumfahrtkongress (2018)

[16] Niemiec R., Gandhi F.: Effects of Inflow Model on Stimulated Aeromechanics of a Quadrotor Helicopter. AHS 72nd Annual Forum (2016)

[17] Leishman J.G.: Principles of Helicopter Aerodynamics. Second Edition. Cambridge University Press (2006)

[18] Tan J., Wang H. Simulating unsteady aerodynamics of helicopter rotor with panel/viscous vortex particle method. Aerospace Science and Technology 30, 255-268 (2013)

[19] Theys B., Dimitriadis G., Andrianne T., Hendrick P., De Schutter J.: Wind Tunnel Testing of a VTOL MAV Pro-

peller in Tilted Operating Mode. International Conference on Unmanned Aircraft Systems (2014)
[20] Kolaei A., Barcelos D., Bramesfeld G.: Experimental Analysis of Small-Scale Rotor at Various Inflow Angles. International Journal of Aerospace Engineering (2018)
[21] Lößle F., Kostek A., Schmid R.: Experimental measurement of a UAV rotor's acoustic emission. Notes on Numerical Fluid Mechanics and Multidisciplinary Design, Vol. (2020)
[22] Lößle F., Kostek A.A., Schwarz C., Schmid R., Gardner A.D., Raffel M.: Aerodynamics of Small Rotors in Hover and Forward Flight. 48th European Rotorcraft Forum, Winterthur, Switzerland (2022)
[23] Abbott I.H., von Doenhoff A.E., Stivers Jr. L.S.: Summary of Airfoil Data. Report Np.824, National Advisory Committee for Aeronautics (1945)
[24] Chen R.T.N.: A Survey of Non-uniform Inflow Models for Rotorcraft Flight Dynamics and Control Applications. NASA Technical Memorandum 102219. (1989)
[25] Mahmuddin F., Klara S., Sitepu H., Hariyanto S.: Airfoil Lift and Drag Extrapolation with Viterna and Montgomerie Methods. Energy Procedia 105, p. 811-816 (2017)
[26] Johnson W.: Helicopter Theory. Dover Publications, Inc., New York (1980)
[27] Ahmed S.R., Vidjaja V.T.: Unsteady Panel Method Calculation of Pressure Distribution on BO 105 Model Rotor Blades. Journal of the American Helicopter Society 43.1, p. 47-56 (1998)
[28] Yin J., Ahmed S.R.: Helicopter Main-Rotor/Tail-Rotor Interaction. Journal of the American Helicopter Society 45.4, p. 293-302 (2000)
[29] Wilke G. et al.: Prediction of Acoustic Far Field with DLR's Acoustic Code APSIM+. (2019)
[30] Mudry, M.: La théorie des nappes tourbillonnaires et ses applications à l'aérodynamique instationnaire, PhD thesis, University of Paris VI (1982)
[31] Gallas Q., Boisard R., Monnier J.-C., Pruvost J., Giliot A.: Experimental and numerical investigation of the aerodynamic interactions between a hovering helicopter and surrounding obstacles, 43nd European rotorcraft Forum, Milan, Italy (2017)
[32] Boisard R.: Aerodynamic investigation of a helicopter rotor hovering in the vicinity of a building. 74th AHS forum, Phoenix, Arizona, USA (2018)
[33] Boisard R.: Numerical Analysis of Rotor / Propeller aerodynamic interactions on a high speed compound helicopter. Journal of the American Helicopter Society, Vol. 67, No. 1, pp. 1-15 (2022)
[34] Prieur J. and Rahier G.: Comparison of the Ffowcs Williams-Hawkings and Kirchhoff rotor noise calculations. 4th AIAA/CEAS Aeroacoustics Conference, Toulouse (1998)
[35] Rahier G. and Prieur J.: An efficient Kirchhoff integration method for rotor noise prediction starting indifferently from subsonically or supersonically rotating meshes. 53rd AHS Annual Forum, Virginia Beach, USA (1997)
[36] Kroll N., Eisfeld B., Bleecke H. M.: The Navier-Stokes code FLOWer. In: Schuller A. (Ed.), Portable Parallelization of Industrial Aerodynamic Applications (POPINDA), Notes on Numerical Fluid Mechanics, Vol. 71, pp. 58-71 (1991)
[37] Kowarsch U., Oehrle C., Hollands M., Keßler M., Krämer E.: Computation of Helicopter Phenomena Using a Higher Order Method. In: Nagel W. E., Kröner D. H., Resch M. M., High Performance Computing in Science and Engineering '13, pp. 423-438 (2013)
[38] Keßler M., Wagner S.: Source-Time Dominant Aeroacoustics. Computers & Fluids. Vol. 33, No. 5-6, pp. 791-800 (2004)
[39] Dürrwächter L., Keßler M., Krämer E.: Numerical Assessment of Open-Rotor Noise Shielding with a Coupled Approach. AIAA Journal. Vol. 57, No. 5. (2019)
[40] Dürrwächter L.: Simulation of Installation Effects on Open-Rotor Acoustics with a Coupled Numerical Tool Chain. PhD thesis. University of Stuttgart (2020)
[41] A. Visingardi, A. D'Alascio, A. Pagano, P. Renzoni, Validation of CIRA's rotorcraft aerodynamic modelling system with DNW experimental data. 22nd European Rotorcraft Forum, Brighton, UK (1996)
[42] Morino, L., A General Theory of Unsteady Compressible Potential Aerodynamics. NASA CR-2464 (1974)
[43] J. E. F. Williams, D. L. Hawkings, Sound generation by turbulence and surfaces in arbitrary motion. Philosophical Transactions of the Royal Society of London. Series A, Mathematical and Physical Sciences 264 (1151) (1969)
[44] D. Casalino, An advanced time approach for acoustic analogy predictions. Journal of Sound and Vibration 261 (4) (2003)
[45] D. Casalino, M. Barbarino, A. Visingardi, Simulation of helicopter community noise in complex urban geometry. AIAA Journal 49 (8) (2011)
[46] M. Barbarino, F. Petrosino, A. Visingardi, A high-fidelity aeroacoustic simulation of a VTOL aircraft in an urban air mobility scenario. Aerospace Science and Technology (2021)
[47] Barbarino M., Bianco D., A bem-fmm approach applied to the combined convected Helmholtz integral formulation for the solution of aeroacoustic problems, Computer Methods in Applied Mechanics and Engineering 342 (2018)
[48] Petrosino F., Barbarino M., Staggat M., Aeroacoustics assessment of an hybrid aircraft configuration with rear-mounted boundary layer ingested engine, Applied Sciences 11 (7) (2021)
[49] Maekawa Z., Noise reduction by screens, Applied Acoustics 1 (3) (1968)
[50] Kurze U. J., Noise reduction by barriers, The Journal of the Acoustical Society of America 55 (3) (1974)
[51] Branlard E.: Tip-losses with Focus on Prandtl's Tip Loss Factor. Wind Turbine Aerodynamics and Vorticity-Based Methods (pp.227-245) (2017)